A single parameter approach to enhance the microstructural and mechanical properties of beta Ti-Nb alloy via open-air fiber laser nitriding

Chi-Wai Chan*[a], Xianwen Chang[b], Mohammad Amin Bozorgzadeh[b], Graham C. Smith[c], Seunghwan Lee[b]*

[a]School of Mechanical and Aerospace Engineering, Queen's University Belfast, BT9 5AH, UK
[b]Department of Mechanical Engineering, Technical University of Denmark, DK-2800 Kgs. Lyngby, Denmark
[c]Faculty of Science and Engineering, University of Chester, Thornton Science Park, Chester CH2 4NU, UK

Abstract

In this study, the idea of applying open-air laser nitriding to improve the microstructural and mechanical properties of beta Ti-45 at.% Nb alloy was demonstrated. Surface cracking after laser nitriding is one of the main reasons impeding direct translation of the laser nitriding technique from the laboratories to industries as cracks can be the weak points to initiate mechanical and corrosion failures in long-term usage. With proper selection of duty cycle (DC) between 40% (modulated mode) and 100% (continuous wave, CW mode) to control the laser energy input and laser-material-gas interaction time, the cracking problems of laser nitriding can be alleviated and even solved. A crack-free and uniformly gold-coloured nitrided surface was successfully obtained at the DC of 40% in this study. The morphology, microstructure, composition and mechanical properties of the nitrided samples were studied and analysed by optical microscopy (OM), scanning electron microscopy (SEM), SEM-energy dispersive X-ray spectroscopy (EDX), X-ray diffraction (XRD) and Vickers micro-hardness tests. The OM results indicated that minimum overlapping between the laser tracks would give desirable results to obtain the crack-free surface. The measurements from the SEM micrographs indicated the depth of the laser-nitrided areas ranged between 22 and 43 μm. The XRD findings showed that a clear conversion of the TiNb surface to a nitride as a result of laser nitriding was observed. The maximum hardness, as measured by the Vickers method in cross-sections, lay in the range of 780 to 870 HV after laser nitriding. To summarise, control of DC to obtain a crack free and quality surface via fiber laser nitriding in open air is a simpler and quicker approach in comparison with the conventional substrate preheating and nitrogen (N) dilution approaches. The single-parameter approach is more efficient than parameter optimisation via design of experiments (DOE) employed in conventional methods.

Keywords: beta Ti-Nb alloys, laser nitriding, fiber laser, titanium nitride (TiN), orthopaedics

Correspondences: Dr. Chi-Wai Chan (c.w.chan@qub.ac.uk); Dr. Seunghwan Lee (seele@mek.dtu.dk)

Credit authorship contribution statement

Chi-Wai Chan: Conceptualization, Formal analysis, Resources, Writing - original draft, Writing - review & editing, Project Administration, Validation, Visualization, Funding acquisition.

Xianwen Chang: Methodology, Formal analysis, Investigation, Data curation, Writing - review & editing

Mohammad Amin Bozorgzadeh: Methodology, Formal analysis, Investigation, Data curation

Graham C. Smith: Formal analysis, Writing - original draft, Writing - review & editing, Validation

Seunghwan Lee: Conceptualization, Resources, Writing - review & editing, Project Administration, Supervision, Funding acquisition.

Research Highlights

1. Fiber laser nitriding with pulsed modulation was used to treat beta TiNb alloy.
2. Duty cycle changed between 40% and 100% to control and optimise surface quality.
3. The nitrided samples had the melt pool depth between 22 and 43 μm.
4. Maximum hardness of the nitrided samples lay within the range of 780-870 HV.
5. Crack-free and homogenous nitrided surface can be created at duty cycle of 40%.

1. Introduction

Implant failure is one of the critical problems for patients who have undergone the total hip replacement (THR). Revision surgery is required to clean or replace the damaged parts if implant failure happened. It is costly and causes pain to the patients. The revision procedures can cost over one billion dollars annually in the US [Katz et al., 2007]. The common reasons for revision surgery are aseptic loosening, bacterial infection, mechanical fracture of parts, as well as a combination of corrosion and wear causing a leak of harmful ions/debris to the bloodstream [Evans et al., 2019]. A recent review provides an estimate from national registries that a hip replacement can last for 25 years [Evans et al., 2019]. However, due to an increasing number of younger and more active patients with THR, it is necessary to prolong the service life of hip implants by finding a safe and durable solution to tackle the aforementioned problems.

Hip implants are composed of a femoral stem with a ball head fitted into an acetabular cup with a liner, to allow free movement between the ball and liner. Depending on material selection (metal/plastic/ceramic) for the stem and ball parts, there are three different constructs: metal-on-metal (MoM), metal-on-plastic (MoP), and ceramic-on-ceramic (CoC). The former refers to the material for the stem whilst the later refers to the ball. It has been newly reported [Pijls et al., 2019] that patients with MoM-THR tended to be younger than patients with standard (or non-MoM) THR. The stem in MoM construct is usually made with Ti6Al4V (grade 5) alloys which have a much higher Young's modulus (110 GPa) compared with cortical bone (10-30 GPa). The mismatch of modulus between the Ti6Al4V stem and human bone is a main reason for aseptic loosening. Furthermore, toxicity of Al and V is another concern of using Ti6Al4V as the stem material. Meanwhile, the ball head is usually made of CoCr, a more wear resistant alloy. The coupling of the femoral head (CoCr) and stem trunnion (Ti6Al4V) has been known as problematic: wear or corrosion (or a combination of both) can happen and is attributable to micro-motions at the head-neck interface, thus releasing the harmful metallic ions or particles into the contacting body fluids [Mistry et al., 2016]. Therefore, there is an urge to identify a biocompatible, completely non-toxic, mechanically strong and chemically stable material as an alternative to replace Ti6Al4V.

Among the potential options within the family of Ti-based alloys, beta TiNb-based alloys show the highest potential over others given their (i) capability to achieve the lowest possible modulus (55 GPa)[Geetha et al., 2009], (ii) composition being non-toxic to the human body [Pilz et al. 2018], as well as (iii) exhibition of shape memory effect and super-elasticity like NiTi alloys [Kim et al., 2006]. However, the TiNb-based alloys have the drawback of poor wear resistance; therefore they cannot be used as the stem component without surface hardening treatment.

Laser surface treatment is one of the most efficient and versatile surface modification techniques to improve the surface performance of materials when compared with other well-established techniques, such as plasma spraying, ion implantation, as well as physical or chemical vapour deposition (PVD or CVD) techniques [Hussein et al. 2018, Zhang et al. 2019, Zhao et al. 2019]. Since firstly reported by Katayama et al. [Katayama et al., 1983], laser nitriding has been proven as a sensible method for enhancing the surface properties of Ti alloys. The advantages include small heat input, fast and clean processing, capability to treat the localised and selected area (without altering the substrate properties) as well as to create a thick (up to a few hundred μm) and metallurgically bonded nitride layer to the substrate. The scientific background of laser nitriding and its development to date have been reported elsewhere [Kamat et al. 2019]. One of the motivations for the continuous development of laser nitriding is driven by hardening the Ti implant surfaces to minimise the wear problems. However, the key barriers that hinder the direct application of laser nitriding to treat the implant

surfaces in industries are (i) requirement of a specific gas/vacuum chamber (usually only applicable to treat flat surfaces) and (ii) crack formation in the nitrided surfaces. The former problem limits the practicality of laser nitriding because hip implant components are free-form (or curved) in shape, whilst the latter induces an uncertainty in the mechanical properties especially in long-term usage (e.g. surface cracks can be a weak point to cause fatigue failure).

Recent research by the authors' group has developed an open-air laser nitriding technique to address the issue of treating the surfaces without the need of a gas/vacuum chamber. The laser-nitrided surfaces have been proven to be highly antibacterial, corrosion and wear-resistant because of the formation of a titanium nitride (TiN) layer. TiN is known to be a very hard and chemically inert. The newly developed technique was successfully applied to different Ti-based materials, e.g. commercially pure (CP) Ti [Chan et al., 2017a, 2017b], Ti6Al4V [Chan et al., 2017a, 2017b] and Ti-Nb-Zr-Ta (TNZT) alloys [Donaghy et al. 2020]. However, these open-air laser nitriding processes were conducted in the continuous wave (CW) mode, and cracks can occasionally appear in the nitrided surfaces.

Several attempts have been reported in literatures to tackle the cracking problems in laser nitriding. They can be categorised into two routes: (i) preheating the substrate [Xue et al., 1997, Hu et al., 1999] and (ii) diluting the N shielding gas with argon (Ar) [Mridha et al., 1994, Nwobu et al., 1999, Kaspar et al., 2007]. Preheating the substrate would unnecessarily lengthen the treatment time and increase the process complexity whilst dilution of N_2 with Ar can lead to reduced hardness of TiN layer because the presence of ionic Ar could minimise N diffusion into the surface [Geetha et al. 2004].

In this study, the main objective is to create a crack-free and homogenously nitrided surface in the Ti 45 at.% Nb alloys using a quick and simple one-step approach. This was achieved by nitriding the TiNb surfaces using parameter control of duty cycle (DC). It is one of the first attempts to study the open-air fiber laser nitriding of TiNb alloys with pulse modulation. The hypothesis is that a crack-free nitrided surface can be produced by performing the open-air laser nitriding at a suitable DC to control the amount of laser energy input and the duration of laser-material-gas interaction time, and thus the rate of chemical reactions between Ti and N in the laser re-melted pools. In other words, this is to minimise the crack formation by controlling the size and population of TiN dendrites in the re-melted pools using an energy control method. It is based on the assumption that the formation of oversized and densely populated TiN dendrites, as a consequence of oversupply of laser energy and prolonged laser-material-gas interaction time, can lead to excessive build-up of residual stress in the re-melted pools and eventually cause cracking [Kamat et al. 2019].

On the other hand, since only one processing parameter (DC) is included, it is obviously simpler than the conventional parameter optimisation approach (which often involves the design of experiments (DOE)) because the complicated interactions between different laser processing parameters can be neglected.

2. Materials and Experiments

2.1. Materials

The materials used: Ti-45 at.%Nb alloy was sourced from the American Elements in the plate form of 250 mm x 250 mm x 2 mm. They were spark cut by wire electrical discharge machining (EDM) into smaller size of 125 mm x 30 mm for laser nitriding experiments. Before the experiments, the sample surfaces were ground and polished using a series of silicon carbide (SiC) sandpapers starting with 120 grit up to 1000 grit. The polished samples were cleaned and degreased in an ultrasonic water bath using acetone for 10 min, followed with rinsing in deionised water and finally dried in a stream of cool air.

2.2. Laser nitriding experiments in open air

The cleaned and dried samples were laser-nitrided in open air using the SPI 200W fiber laser machine. The laser machine was integrated by Micro Lasersystems BV (Driel, Gelderland, the Netherlands) and the fiber laser with 1064 nm in wavelength was manufactured by SPI Lasers UK Ltd (South Hampton, Hampshire, UK). The laser machine can be working in CW and modulated modes (modulated to 100 kHz, modulated pulses <5µs to CW). The laser processing parameters were selected in accordance with a set of preliminary experiments, and they were set at 45 W (laser power), 40% to 100% (duty cycle, DC), 25 mm/s (laser scanning speed), 1.5 mm (stand-off distance, SD or the distance between the laser nozzle and the sample surface), and purging with pure N_2 gas at a gas pressure of 6 bar delivered coaxially with the laser beam. The laser spot size at the SD of 1.5 mm was calculated to be 100 µm. DC was the only parameter being varied in the laser nitriding experiments, whilst the other parameters were kept constant.

DC is the ratio of the ON time to total time (ON + OFF). DC of 40% means for 40% of the total time the laser was in the ON state, whilst DC of 100% is the CW mode with which the laser was always in the ON state. The samples were denoted as DC40, DC60, DC80 and DC100 to represent the samples nitrided at DC of 40%, 60%, 80% and 100% hereafter. The schematic of the laser nitriding setup was reported elsewhere [Chan et al., 2017b]. The size of the nitrided areas was 10×10 mm^2 encompassing of around 100 laser tracks. Each DC condition was repeated six times to ensure repeatability (given in Fig. 1).

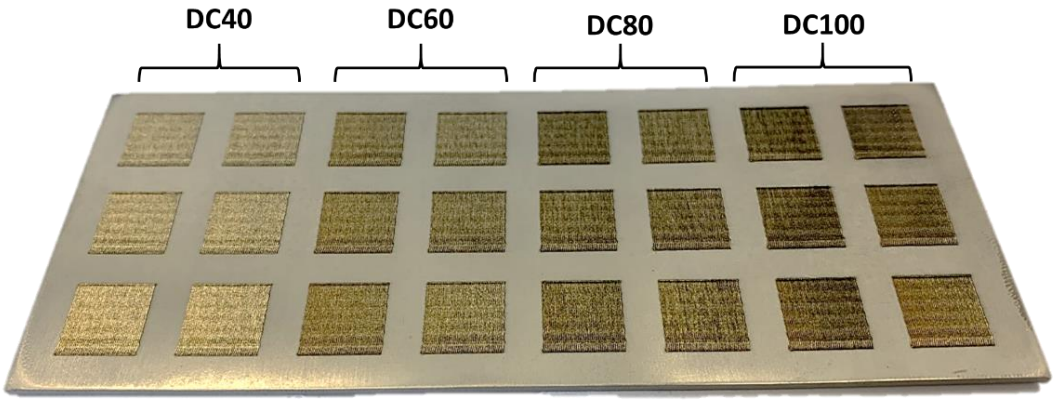

Fig. 1. Ti-45 at.% Nb plates laser-nitrided with different DC between 40% and 100%. Each condition was repeated six times (n = 6)

2.3. Morphology and composition analysis

The morphology of the top and cross-sectioned surfaces after laser nitriding was captured using a standard optical microscope (OM) and scanning-electron microscope (SEM, FlexSEM 1000, Hitachi, UK). Standard metallurgical procedures were applied to prepare the cross-sectioned samples for imaging. The SEM was operated at both the secondary-electron (SE) and backscattered electron (BSE) modes using a 20-kV beam for capturing the top surface morphology and cross-sectioned microstructure at higher magnifications. The compositions at the top and cross-sectioned surfaces were analysed using the same SEM machine equipped with energy-dispersive X-ray spectroscopy (EDX). The elemental compositions were measured and quantified in at%, and the distribution of elements were visualised using EDX mapping.

2.4. Phase structure analysis (for top surface)

The X-ray diffractometer (XRD) (PANanalytical X'Pert Pro MPD, PANalytical, UK) was used to identify the phases of the surfaces nitrided at different DC conditions. The untreated sample was used as a control. The surfaces were characterised by XRD in the following setting: 2θ angle range between 10° - 90° with a copper-Kα radiation source (40 kV and 40 mA) and nickel filter operated at fixed slit (½°), 10° anti-scatter slit and 0.02 step size.

2.5. Vickers micro-hardness measurements (in cross-sectioned surface)

The Vickers hardness tester (Future-Tech Corp FM-700, Japan) was used to measure the micro-hardness in cross-sections of the samples. A total of five indentation marks with a separating distance of 15 μm were imprinted in the cross-sectioned surfaces. The first indentation mark was located 15 μm below the top surface. A load of 10 kgf with a dwell time of 10 s was applied at each indentation. The measurements were repeated at least three times (n = 3) to ensure repeatability and to calculate the mean and standard error (SE) of hardness.

3. Results and Discussion

3.1. Top surface morphology captured using optical microscope (OM)

Fig. 2(a-b) shows the top surface morphology for the samples laser-nitrided at different duty cycle conditions with different magnifications (x10 and x40). As can be seen from Fig 2b(i-iv), successive and overlapped laser-nitrided tracks were found on the surfaces. The width of each track in the samples was about 100 μm (similar to the laser spot size) but the extent of overlapping between the laser tracks varied with different conditions. Fig. 3 shows the overlapping percentage (calculated by using ImageJ software) of laser tracks for DC40 to DC100. DC40 had the lowest overlapping percentage of 5.4%. It increased with increasing duty cycle and reached the highest of 24.8% in DC100. Within each track, the moving pattern of laser spots after re-solidification (i.e. overlapped crescents) was observable.

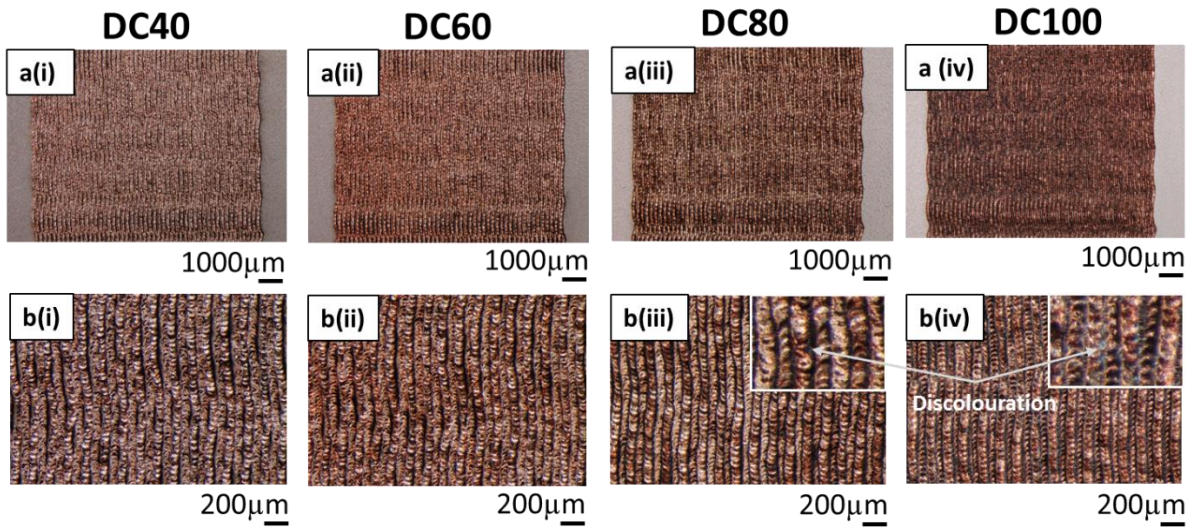

Fig. 2(a-b). The optical micrographs (OMs) showing the top surface morphology for the laser-nitrided samples treated at different duty cycles: DC40, DC60, DC80 and DC100. Fig. 2a (i-iv) show the OMs magnified at x10 while Fig. 2b (i-iv) show the OMs at higher magnification of x40. The insets in Fig. 2b(iii and iv) depict the areas with surface discolouration in DC80 and DC100.

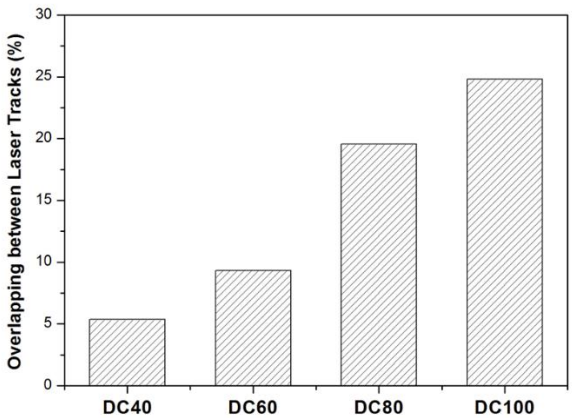

Fig. 3. The overlapping percentages between the laser tracks of different laser-nitrided samples. The measurements were taken from Fig. 2b using ImageJ software.

A light gold coloured surface was observed on DC40 and DC60, whilst DC80 and DC100 showed a dark gold surface in a background of brown and/or blue colours in some regions (highlighted in the insets in Fig. 2b(iii-iv)). With increasing duty cycle from DC40 to DC100, the trend of colour darkening was apparent. The presence of gold colour was due to the formation of titanium nitride (TiN) in the surfaces after laser nitriding [Chan et al., 2017a, 2017b]. The darkening in gold colour across the sample surfaces indicates different amount of nitrogen (N) intake in the surfaces. The higher the N intake in the surface, the darker is the surface.

The appearance of brown and blue colours in DC80 and DC100 was attributed to the intrusion of surrounding air in the open-air nitriding process, leading to oxygen (O) contamination in the surfaces. It has been previously reported that TiN can react with O to form different oxides, i.e. TiO_2 and TiNxOy [Chan et al., 2017b]. Colour of these surface oxides varies with the thickness as a consequence of the light interference phenomena at the metal-oxide-air interfaces [Diamanti, et al. 2008]. It also indicates that laser nitriding at higher duty cycles, namely DC80 and DC100, created oxide layers with heterogeneous thickness. In contrast, the thickness of oxide layers in DC40 and DC60 were more homogeneous as reflected by the more uniform gold colour throughout the surfaces.

3.2. Cross-sectioned profile captured by OM

The micrographs of cross-sectioned surfaces for different samples are depicted in Fig. 4(i-iv). The depth of the laser re-melted pools measured from Fig. 4 using ImageJ software (n = 3) is given in Fig 5. The depth was defined as the distance from the top surface down to the bottom of the re-melted pools.

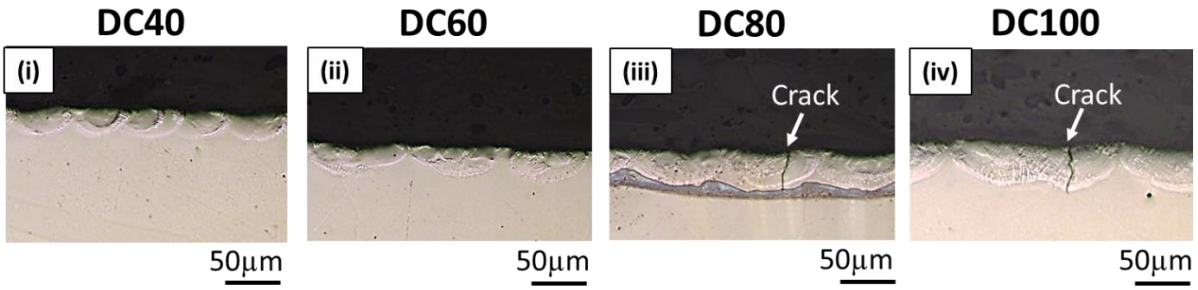

Fig. 4(i-iv). The OMs showing the cross-sectioned profiles of different laser-nitrided samples. Macro-cracks in DC80 and DC100 are pointed by the arrows in Fig. 3(iii-iv).

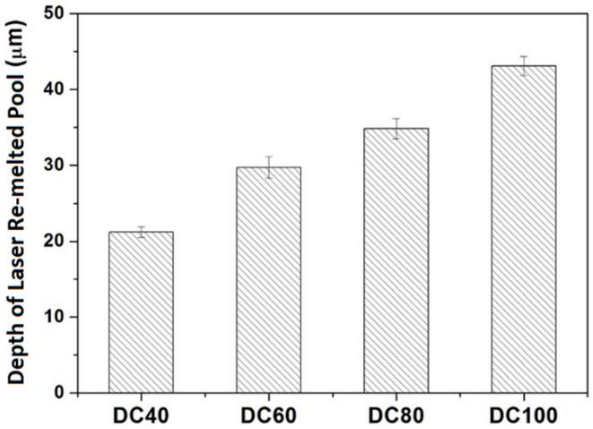

Fig. 5. The depth of laser re-melted pools measured from the cross-sectioned profiles (n = 5) in Fig. 3 using ImageJ software.

Semicircular shaped re-melted pools were observable from all samples in Fig. 4. As seen in Fig. 5, the depth of the re-melted pools increased linearly with increasing duty cycles. The depth was sized between 22 and 43 μm. No cracks were seen in DC40 and DC60, whilst macro-cracks which grew perpendicular to the surface and reached to the bottom of the re-melted pools were present in DC80 and DC100. It has been reported by Kloosterman and Hosson [1995] that laser treatment of Ti materials created residual stress in the surface. The formation of ceramic and hard materials (i.e. TiN) can cause embrittlement leading to cracking in the surface provided that they are over-grown or populated in the re-melted pool.

Furthermore, overlapping of laser tracks can lead to significant build-up of residual stress in the surface, and thus increase the tendency of cracking (served as a way to relieve residual stress). A research conducted by Xue et al. [1997] reported that the residual stress in the laser-nitrided layer of Ti6Al4V was measured to be tensile, and the magnitude of the residual tensile stress, along and perpendicular to the laser scanning direction, was different (i.e. 950 and 850 MPa along and perpendicular to the direction, respectively).

3.3. Top surface morphology by SEM

Fig. 6(a-b) show the SEM micrographs (x300 and x3000) for the top surface morphology of different laser-nitrided samples. The higher magnification SEMs in Fig. 6b(i-iv) are the enlargement of the selected areas in Fig. 6a(i-iv) showing the presence of micro-cracks in surfaces.

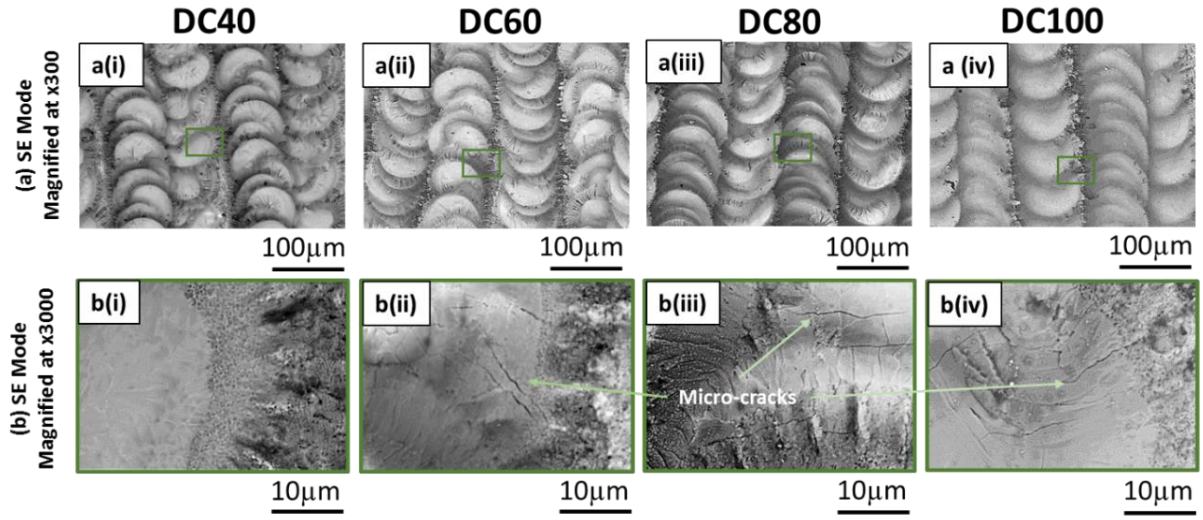

Fig. 6(a-b) showing the SEMs taken at SE mode for the top surface morphology of different laser-nitrided samples. Fig. 6a(i-iv) provide the SEMs magnified at x300 whilst Fig. 6b(i-iv) depict the enlarged views (x3000) selected from Fig. 6a(i-iv) (indicated by the rectangular boxes).

It is noteworthy to point out that the laser-nitrided TiNb surfaces were free of identifiable micro-features (i.e. lamellae and ripples) associated with laser nitriding. This can be attributed to the differences in material properties (e.g. surface tension and viscosity in liquid phase) and the use of different setting of processing parameters (i.e. duty cycle). The presence of these surface features was related to the surface tension and viscosity of liquid Ti as well as the velocity of Marangoni convection in the melt pool. The formation mechanisms of these features were reported elsewhere [Chan et al., 2017b].

Even though cracks of identifiable size (or macro-cracks) were not observed from the OM cross-sectioned profile of DC60 (in Fig. 4(ii)), micro-sized cracks still appeared on the top surface (Fig. 6b(ii)).

Micro-cracks can be observed in the top surfaces of DC80 and DC100 (Fig. 6b(iii-iv)). The size of these micro-cracks was between 10 and 20 µm. The mico-cracks grew perpendicular to the laser scanning direction and extended from the edge to the centre of the laser re-melted spots. Top surface of DC40 was free from micro-cracks. This points to the fact that overlapping between successive laser tracks should be controlled to be less than 5.4% (above which cracking can occur).

3.4. Cross-sectioned microstructure by SEM

Fig. 7(i-iv) shows the SEM micrographs of cross-section profiles for another set of samples. The semicircular shaped laser re-melted pools in different size can be clearly observed in all samples in the SEM micrographs as well. The magnified views of re-melted pools of DC60 and DC100 are shown in Fig. 8 (a-b). The areas selected for magnified views are indicated by the rectangular boxes in Fig. 7(ii) and 7(iv), representing the regions at different depths along the re-melted pools.

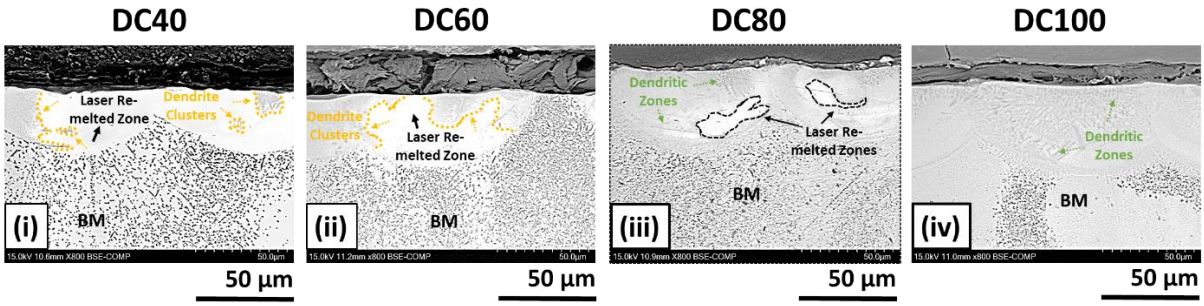

Fig. 7(i-iv) showing the SEMs taken at BSE mode (x800) for the cross-sectioned profiles of different laser-nitrided samples. The dendrite clusters are indicated by the dash arrows and lines (in orange colour) in Fig. 7(i-ii) for DC40 and DC60, whilst the dendrite zones in DC80 and DC100 are indicated by the dash arrows (in green colour) in Fig. 7(iii-iv). The dendritic zone refereed to the interconnected dendrite clusters. The laser re-melted zones in the pools are indicated by the black solid arrows and/or black dash lines in Fig. 7(i-iv). The re-melted zones refer to the areas after melting and re-solidification but without formation of dendrites in recognizable size.

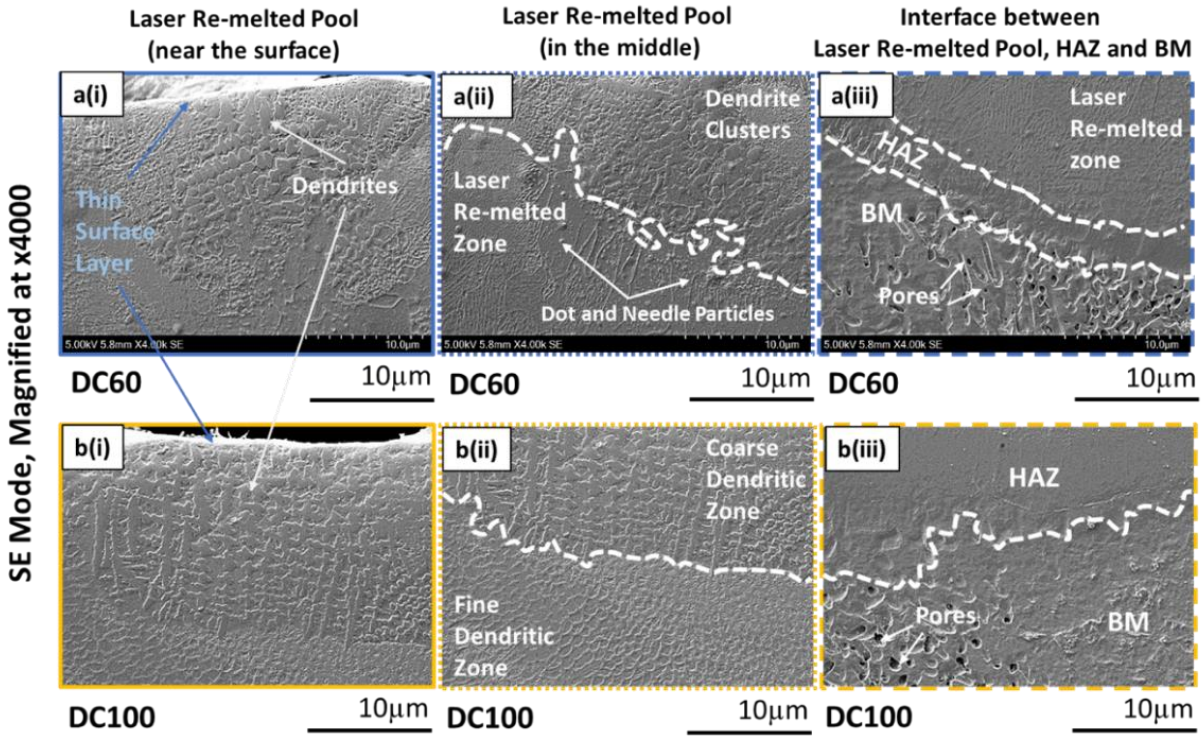

Fig. 8(a-b) showing the higher magnification SEMs taken at SE mode (x4000) for the cross-sectioned profiles of DC60 (Fig. 8a) and DC100 (Fig. 8b) at different depths in the re-melted pool: (i) near the top surface, (ii) in the middle, and (iii) interface between the re-melted pool, HAZ and BM.

For DC40, majority of the re-melted pool areas were dominated by the re-melted zone (indicated by black solid arrows in Fig. 7(i)) whilst some dendrite clusters (orange dash arrows and lines in Fig. 7(i)) appeared just below the surface layer (pointed by the arrows in Fig. 7(i)). The re-melted zone refereed to the areas after melting and re-solidification but without formation of dendrites in recognizable size. The size and population of the dendrite clusters increased when the sample was treated at a higher duty cycle of DC60 (Fig. 7(ii)). On the contrary, majority of the re-melted pool areas in DC80 and DC100 were predominantly occupied by the dendritic zones (pointed by green dash arrows in Fig. 7(iii-iv)). The dendritic zone refereed to the interconnected dendritic clusters. Furthermore, a thin surface layer (in white colour) of 1-2 μm, situated at the topmost surfaces of re-melted pools, can be found from all samples.

The size and population of dendrites in the re-melted pool are related to the amount of N intake, laser-material interaction time and the amount of laser energy input during laser nitriding. With sufficient interaction time, N intake and laser energy input, the dendrites would grow larger and become more densely populated in the re-melted pool. The SEM micrographs in Fig. 7 indicate that the dendrites were not homogenously formed in the re-melted pool. They formed in clusters below the surface layer. Distribution of the dendrite clusters were controlled and determined by the Marangoni convection currents during the re-melting and re-solidification processes. It is believed that DC60 is the threshold condition above which substantial formation of dendrite clusters and significant growth of dendrites would happen. The dendrite clusters, which were composed of large dendrites, would then interconnect with the clusters nearby to form the dendrite zone. This could potentially lead to the built-up of excessive residual stress in the re-melted pool, resulting in the formation of macro-cracks (as seen in Fig. 7).

It can be observed in Fig. 8a(i) that the dendrite clusters in DC60 consisted of dendrites of different sizes, ranging from 0.5 to 3 μm. The dendrites grew in different orientations. In comparison, the dendrites in DC100 (Fig. 8b(ii)) were larger in size (between 2 and 8 μm), and preferably oriented perpendicular to the surface layer. This finding was in agreement with the reported literature using CW mode lasers for laser nitriding of Ti materials [Xin et al., 2000, Man et al., 2003, Abboud at al., 2008, Biswas et al., 2008, Zhao, et al. 2018]. When looking at the deeper region in Fig. 8a(ii), a clear transition between the dendrite clusters and the re-melted zone in DC60 can be seen. The transition line was irregular and a complex network microstructure (comprising particles in needle or dot shape inside a network structure) can be observed. Likewise, a transition line existed between the coarse and fine dendritic zones in DC100 (Fig. 8b(ii)). The dendrites in the fine dendritic zone were about 1 μm in length. However, the transition line in DC100 was more regular compared with that in DC60, indicating more stable thermochemical reactions occurred in the re-melted pool during the laser nitriding process.

As seen in Fig. 8a(iii) and 8b(iii), HAZ can be identified between the re-melted zone and BM in both DC60 and DC100, with a larger size of HAZ in DC100. HAZ is a non-melted region in BM with microstructural changes (e.g. grain size) as a consequence of being exposed to high temperatures. In comparison with DC60, larger HAZ in DC100 indicates a higher amount of heat input to the substrate along with longer interaction time in the re-melt pool, leading to prolonged exposure of the substrate materials to high temperatures.

On the other hand, pores of different sizes can be found in the BM. Porosity, usually caused by gas bubbles from excessive N in the re-melted pool, is a main issue in laser nitriding. Similar to cracking, it is considered to be a defect that can reduce the mechanical properties of the nitrided materials. Pores were absent from the re-melted pools of the nitrided samples, indicating N absorbed in the re-melted pools during laser nitriding, completely reacted with the substrate Ti material to form different TiN compounds, e.g. the known TiN surface layer and TiN dendrites, as well as N-rich Ti solid solutions. There is a possibility of N to react with Nb to form Nb-based nitride compounds or solid solutions but further in-depth investigation is still required for confirmation.

3.5. Top surface and cross-section composition analysis by SEM-EDX

The quantitative measurements of compositions for different samples in the top surfaces are given in Table 1. Fig. 9. shows the mapping results of elemental compositions in the top surfaces.

Table 1 - Quantitative measurements of compositions (at.%) for different samples in the top surfaces

Sample (measurements taken from the red box of SMEs)	EDX Measurements in Top Surface Elemental Composition (at. %)	
	Ti	Nb
BM	30	23.5
DC40	29.8	14.1
DC60	28.3	10
DC80	29.2	10.1
DC100	33.8	5

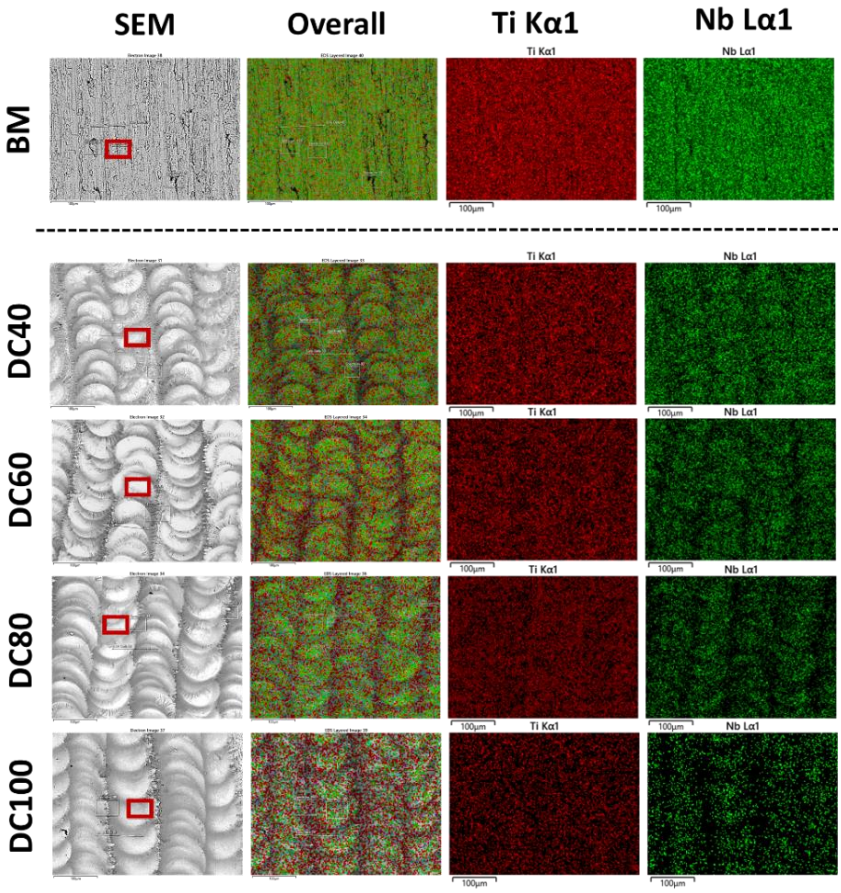

Fig. 9. EDX elemental composition measurements in the top surfaces of different samples. The mapping results for the metallic elements: Ti and Nb in the top surfaces are represented by different colours. The quantitative measurements in Table 1 was carried out in the centre region of laser tracks.

It can be observed from Fig. 9 and Table 1 that when compared with BM, the amount of Nb was reduced after laser nitriding. In general, the reduction of Nb in the laser-nitrided surfaces followed a simple linear relation with the duty cycles (i.e. decreased from 18.8% in DC40 to 5% in DC100). It is particularly important to note that Nb showed a preferential distribution in the laser-nitrided surfaces. Nb was found to be preferably located in the centre region of laser tracks whilst the boundary between laser tracks was depleted of Nb. This observation was more apparent in the surfaces which nitrided at higher duty cycles (DC80 and DC100). Regarding the amount of Ti in the laser-nitrided surfaces, it ranged between 28.3% and 33.7% which is similar to that found in BM (i.e. 30%). It is found to be slightly fluctuating with increased duty cycles. No specific trend can be observed. The most notable finding is that DC100 had the highest amount of Ti in its surface, which is obviously higher than other laser-nitrided samples. The distribution of Ti in the top surfaces after laser nitriding was more homogenous compared with that of Nb. The light elements, such as O and N were not included in the quantification in the EDX surface analysis because the cross-sections for X-ray emission from light elements are much lower than for the typical metallic elements, therefore signals are weaker and more prone to errors in intensity measurement.

The quantitative measurements of compositions for different samples in the cross-sections are given in Table 2. Fig. 10 shows the mapping results of elemental compositions in the cross-sections.

Table 2 - Quantitative measurements of compositions (at.%) for different samples in the cross-sections

Sample (measurements taken from the red box of SEMs)	EDX Measurements in Cross-section Elemental Composition (at. %)	
	Ti	Nb
DC40	38.3	46.9
DC60	37.5	48.3
DC80	33.7	47.7
DC100	33.8	51.3

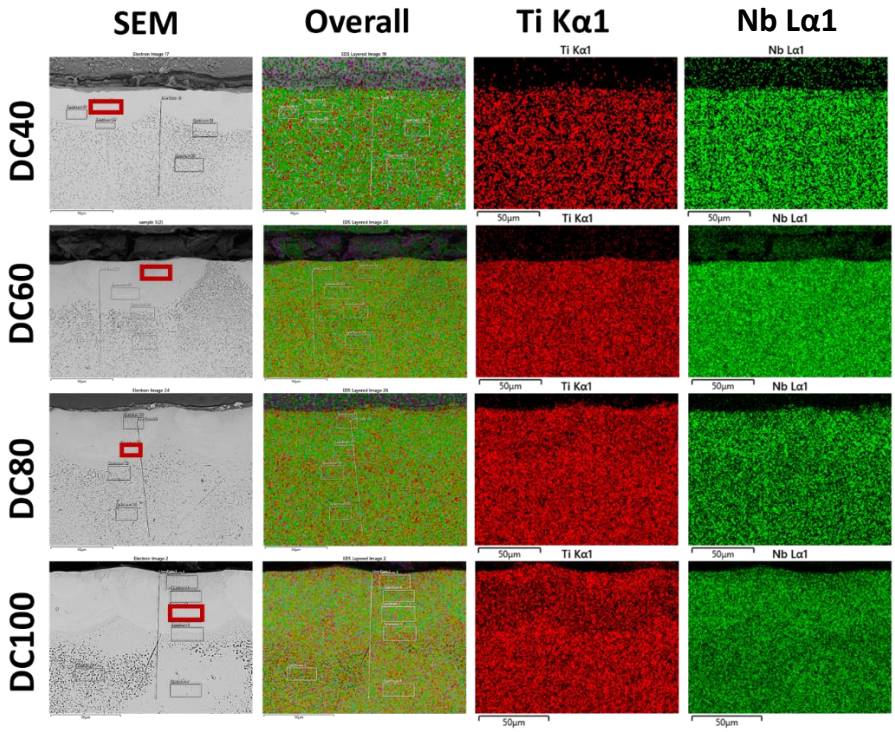

Fig. 10. EDX elemental composition measurements in the cross-sectioned surfaces of different samples. The mapping results for Ti and Nb in the cross-sections are represented by different colours. The quantitative measurements in Table 2 was carried out inside the re-melted pools.

As can be seen in Fig. 10 and Table 2, the cross-sections of DC40 and DC60 had a higher Ti percentage compared with those of DC80 and DC100. Furthermore, when compared with the top surfaces, a higher amount of Ti was found in the cross-sections. It held true for the samples of DC40 to DC80. This can be explained by the fact that the surfaces were significantly enriched with N due to the presence of TiN layer, whilst the amount of N in the interior of re-melted pools was much less when compared with the surfaces, and thus the relative ratio of Ti became higher. Nitriding the samples with higher duty cycles (DC80 and DC100) resulted in a higher amount of N diffused into the re-melted pools to form the TiN dendrites, and hence the fraction of Ti was found be reduced in comparison with DC40 and DC60. The formation of more TiN dendrites in the re-melted pools of DC80 and DC100 is evidenced by the SEM micrographs in Fig. 7 and Fig. 8. It is important to note that DC100 had the same amount of Ti in its top surface and cross-section, both of which equated to 33.8%, indicating the thermochemical reactions of laser nitriding reached to equilibrium with homogenous formation of TiN down from the surface to the inferior regions of the re-melted pool.

Likewise, the amount of Nb was higher in the cross-sections when compared with that in the top surfaces. It can be observed from the mapping results of Nb in Fig. 10 that the interior regions of re-melted pools of DC80 and DC100 had a higher amount of densely-populated green pixels compared with the region (BM) below the re-melted pools. The enrichment of Nb in the interior regions can be attributed to two causes: (i) inward diffusion of Nb and (ii) Marangoni convection currents that transported Nb from the top surfaces to the interior regions of re-melted pools.

3.6. Top surface phase structure analysis by XRD

The XRD data from 20° to 100° diffraction angle, and the expanded scale of selected diffraction angle ranges are shown in Figure 11(a-d) for the BM and the samples nitrided with different duty cycles.

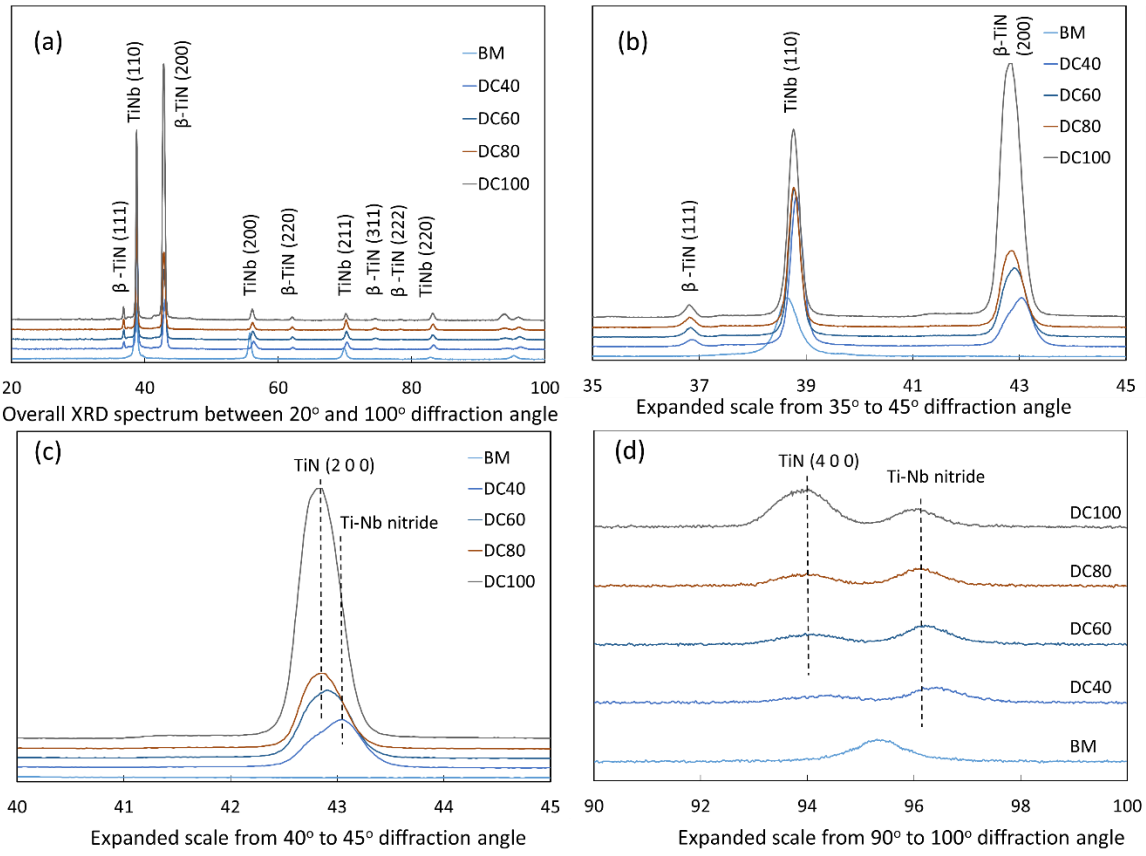

Fig. 11(a-d). The XRD data from BM and different laser-nitrided samples: (a) overall spectrum between 20° and 100° diffraction angle, (b) expanded scale from 35° to 45° diffraction angle, (c) expanded scale from 40° to 45° diffraction angle, and (d) expanded scale from 90° to 100° diffraction angle

The principal phases contributing to the diffraction intensities are labelled in accordance with "star" quality reference data from [International Centre for Diffraction Data] summarised in Table 3. Note that the only phases detected by XRD were those with cubic symmetry; there was no evidence for the presence of hexagonal, orthorhombic or other phases in the XRD data.

Table 3 - Selected reference line positions for the cubic crystalline phases of Ti, Nb, Ti-Nb and TiN. The numerical values are 2θ diffraction line angles for Cu Kα radiation and the lower case letters give an approximate indication of relative intensity: *s = strong, m = medium, w = weak.*

PDF reference	**Phase**	**Diffraction line**							
		(110)	**(200)**	**(211)**	**(220)**	**(311)**	**(222)**	**(310)**	**(400)**
01-074-7075	β-Ti	38.31 s	55.29 w	69.27 m	82.03 w			94.39 w	
00-034-0370	Nb	38.51 s	55.59 m	69.68 m	82.54 w			95.02 w	
01-071-9955	Ti-Nb	38.72 s	55.92 m	70.09 m	83.06 w			95.68 w	
00-038-1420	TiN	36.66 s	42.6 s		61.81 m	74.07 m	77.96 m		93.17 w
01-071-0299	$TiN_{0.9}$	36.69 s	42.62 s		61.86 m	74.12 m	78.02 m		93.25 w
01-089-6042	$NbN_{0.844}$	35.49 s	41.17 s		59.63 m	71.32 m	75.02 m		89.36 w

The untreated BM provides data in very good agreement with the reference data for $Ti_{50}Nb_{50}$, with a main peak corresponding to reflection from (110) planes at 38.7° and weaker peaks visible at 55.9° (200), 70.1° (211), 83.1° (220) and 95.7° (310). After laser nitriding, these peaks are reduced in intensity and suffer small shifts in diffraction angle, and additional peaks are seen due to the presence of a nitride layer. These additional peaks correspond well to reference data for cubic TiN, and are labelled as such in Figure 11(a).

However, close inspection reveals detailed information on the structural changes taking place during the laser nitriding. Figure 11(b) shows the diffraction data on an expanded scale from 35° to 45° diffraction angle. The peak due to (111) reflections from β-TiN remains constant at 36.86 – 36.91° with increasing duty cycle. However, the TiNb (110) peak shows a shift from approximately 38.6° to higher values in the range 38.8 – 38.9° with laser nitriding, indicating a small reduction in interplanar spacing. This is consistent with the shift to higher angle when comparing reference data for the (110) reflection from β-Ti to the equivalent TiNb phase as shown in Table 3. The 40 – 45° range is shown on a further expanded scale in Figure 11(c). The peak due to reflections from the (200) nitride phase is not present in the BM (as expected). This peak was found at approximately 43.0° on the DC40 sample, with a shoulder at approximately 42.8°. With increasing duty cycle, this shoulder was observed to develop into the main contribution to the peak. This indicates that the dominant nitride phase after the laser nitriding at higher duty cycles had a slightly enlarged lattice constant compared to that first formed. The two phases are identified as TiNb-nitride and TiN, by comparison with the trend in the data for β-Ti to the equivalent TiNb phase.

Further evidence for these changes is seen in the expansion to 90 – 100° diffraction angle shown in Figure 11(d). The data show the expected TiNb (310) reflection at approximately 95.4°. The laser nitriding causes this reflection to split into two components at approximately 94.0° and 96.3°, with the 94.0° peak showing an increase in intensity with increasing duty cycle, and the 96.3° peak showing an initial increase followed by a gradual reduction with increasing duty cycle of laser nitriding. The

94.0° peak may be attributed to reflection from the TiN (400) planes. By analogy with the lower angle data, the 96.3° peak can be attributed to similar reflections but in this case from a nitrided TiNb phase. The difference in angle between the 94.0° and 96.3° peaks corresponds to a difference of only 0.3 pm in interplanar spacing, at which point precise interpretation becomes difficult.

3.7. Cross-section surface hardness measurements by Vickers micro-hardness tests

Fig. 12 provides the results of Vickers micro-hardness measured at different cross-section depths (from 10 to 70 μm down to the surface) for different laser-nitrided samples.

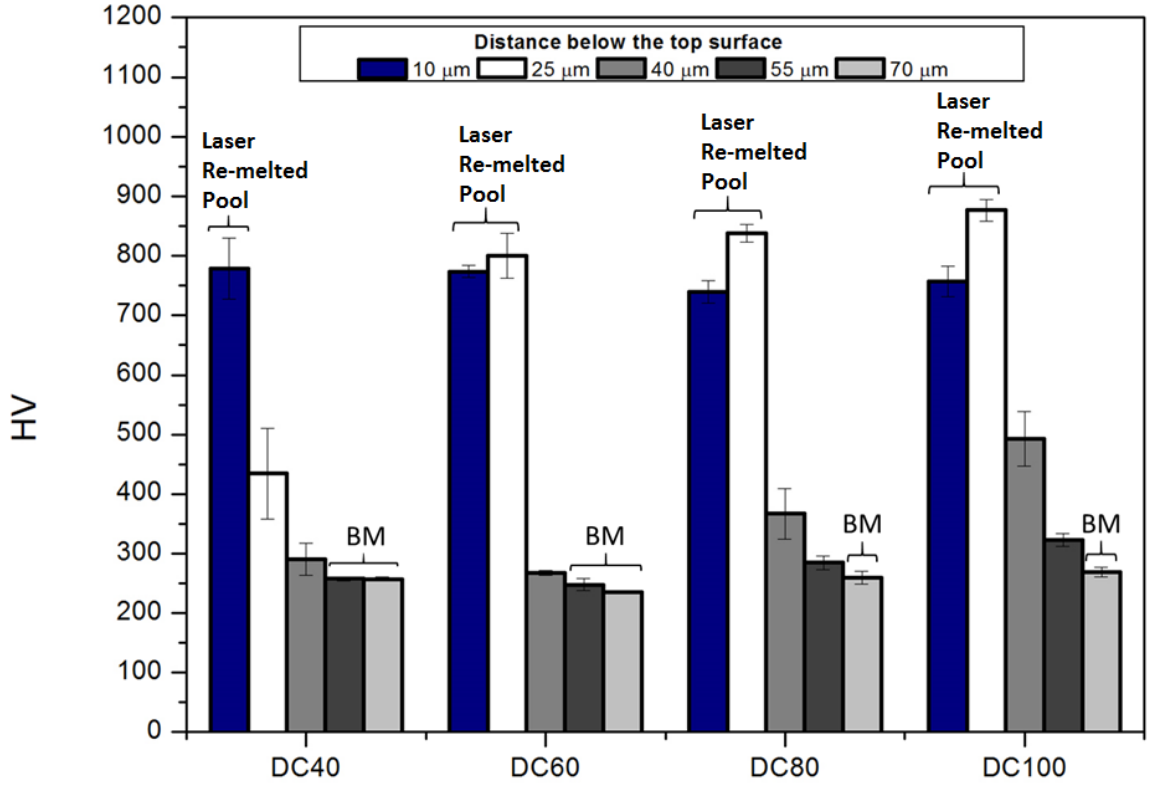

Fig. 12. The Vickers micro-hardness results for different laser-nitrided samples. The micro-hardness for the regions of laser-remelted pool and BM are labelled in the chart.

The maximum hardness of the nitrided surfaces treated by different duty cycles was between 780 and 870 HV, indicating that the hardness difference between the samples was not much. The maximum hardness values lay in the range of the hardness results reported by Sathish et al. [2010]. They reported that the laser-nitrided Ti-13Nb-13Zr alloys, when processed at the higher scanning speed of 720 mm/min (or 12 mm/s), had a hardness of 784 HV.

When looking into the hardness of individual samples, the maximum hardness for DC40 was located at the depth of 10 μm (still within the depth of re-melted pool as given in Fig. 5). The hardness significantly dropped to 440 HV at the depth of 25 μm, and reached the minimum of 250 HV at the depth of 55 μm and below (in the region of BM). Regarding the hardness profile of DC60, the hardness at the depths of 10 and 25 μm was similar to each other (i.e. between 770 and 800 HV). The depth of re-melted pool in DC60 was 30 μm, indicating the two hardness measurements were taken within the region of the re-melted pool. The hardness was significantly reduced to about 250 HV at a depth of 40 μm and below. The hardness profiles for DC80 and DC100 behaved similarly to each other. The hardness at the depth of 10 μm is lower than that of 25 μm, and the measurements were taken within the re-melted pools of DC80 and DC100 (i.e. 35 and 43 μm, respectively). There is a noticeable drop

of hardness at the depth of 40 μm, and the hardness continued to decrease until it reached the minimum of about 250 HV at the depth of 70 μm.

It is important to note that the hardening mechanisms for the samples treated at higher (DC80 and DC100) and lower (DC40 and DC60) duty cycles were different. With regard to DC40 and DC60, the hardening in the re-melted pools was mainly due to the contributions from the clusters of small TiN dendrites and nitrogen-rich Ti, as can be seen from the SEM micrographs in Fig. 7(i-ii). Furthermore, the contribution from the nitrogen-rich Ti would be more significant than that of dendrite clusters, as the population of dendrite clusters in the re-melted pools was small. In addition, other interstitial alloying elements, such as O, can contribute to the hardening effect. O is a solid solution strengthener in Ti [Collings, 1984]. A research conducted by Kim and Miyazaki [2016] showed that the increase of O content in the TiNb alloys can increase the yield stress. Since the laser nitriding was conducted in an open-air condition, O in the surrounding atmosphere can intrude into the re-melted pool due to turbulence flow. This is evidenced by the surface discolouration in Fig. 2. O from the surface can be transferred to the interior of re-melted pools by diffusion at elevated temperatures. It can also reach the deeper pool areas by convection currents, allowing the possibility to react with the re-melted materials, namely Ti and Nb. Precipitation of the needle and dot shaped particles (as shown in Fig.7 a(ii)) can also contribute to the increase of hardness. It has been reported by Geetha et al. [2004] that the needle-like structures contained a mixture of TiN phases (cubic and hexagonal) and martensitic Ti (α'-Ti).

On the other hand, the hardness enhancement in DC80 and DC100 was mainly attributed to the formation of dendritic zones (or interconnected dendrite clusters) in the re-melted pools. The nitrogen rich Ti also contributed to the hardening effect but to a less extent. Furthermore, the higher hardness recorded at the depth of 10 μm than that of 25 μm was attributed to the differences in grain size between the coarse and fine dendritic zones. As seen in the magnified SEM micrographs for DC100 (in Fig. 8b(i)), the coarse dendritic zone only reached the depth of around 16 μm in the re-melted pool, below which was the fine dendritic zone. It is believed that the hardness measurement at the 10 μm depth was inside the coarse dendrite zone (dendrites sized between 2 and 8 μm) and that at 25 μm depth was inside the fine dendrite zone (dendrites sized about 1 μm). According to the Hall-Petch effect, the hardness and strength increased with decreasing grain size. The effect is valid for the materials with grain sizes ranging from one millimetre down to one micrometre [Petch, 1953]. Therefore, it was not surprising to see this phenomenon (i.e. hardness at the measurement depth of 25 μm higher than that of 10 μm in DC80 and DC100).

It is important to note that the TiN surface layer (1-2 μm thick) was too thin to contribute to the hardening effect of re-melted pools measured in their cross-sections.

4. Conclusions

A crack-free and homogenous nitrided surface of Ti 45 at.%Nb alloy was successfully created by open-air fiber laser nitriding with pulse modulation (by control of duty cycle). The important findings as follows:

1) Duty cycle of 40% (DC40) was found to be the optimal condition to create the crack-free and uniformly gold-coloured surface. Overlapping area between the successive laser tracks was critical to obtain the crack-free surface. Minimum overlapping would give desirable results.
2) The depth of laser re-melted pools in the nitrided samples ranged between 22 and 43 μm.
3) A clear conversion of the TiNb surface to a nitride as a result of laser nitriding was observed. There is evidence to indicate the initial conversion at DC40 was to a mixed Ti-Nb nitride, but that the proportion of Nb was reduced with increased duty cycle. At higher duty cycles, the resulting nitride layer had a high proportion of TiN. There is no indication of phases other than cubic i.e. β phases in the Ti or TiNb alloy.
4) The maximum hardness in cross sections lay in the range of 780 to 870 HV after laser nitriding. The hardness increment was in a close relation to the size of TiN dendrites in the re-melted pools. The smaller the dendrites the higher was the hardness.

Acknowledgement

This work was supported by research grants from the Queen's University Belfast, awarded to C-WC (D8201MAS).

5. References

[1] Katz, J.N., Wright, J., Wright, E.A., Losina, E., Failures of total hip replacement: a population-based perspective, The Orthopaedic Journal at Harvard Medical School, 9 (2007) 101-106.

[2] Evans, J.T., Evans, J.P., Walker, R.W., Blom, A.W., Whitehouse, M.R., Sayers, A., How long does a hip replacement last? A systematic review and meta-analysis of case series and national registry reports with more than 15 years of follow-up. Lancet 393 (2019) 647-654.

[3] Pijls B.G., Meessen J.M.T.A., Tucker K., Stea S., Steenbergen L., Fenstad A.M., Mäkelä K., Stoica I.C., Goncharov M., Overgaard S., de la Torre J.A., Lubbeke A., Rolfson O., Nelissen R.G.H.H., MoM total hip replacements in Europe: a NORE report, EFORT Open Reviews 4(6) (2019) 423-429.

[4] Mistry, J.B., Chughtai, M., Elmallah, R.K., Diedrich, A., Le, S., Thomas, M., & Mont, M.A., Trunnionosis in total hip arthroplasty: a review. Journal of orthopaedics and traumatology: official journal of the Italian Society of Orthopaedics and Traumatology, 17(1) (2016) 1-6.

[5] Geetha, M., Singh, A.K., Asokamani, R., Gogia, A.K., Ti based biomaterials, the ultimate choice for orthopaedic implants – a review, Progress in Materials Science, 54 (2009) 397-425.

[6] Pilz, S., Gebert, A., Voss, A., Oswald, S., Göttlicher, M., Hempel, U., Eckert, J., Rohnke, M., Janek, J., Calin, M., Metal release and cell biological compatibility of beta-type Ti-40Nb containing indium, Journal of Biomedical Materials Research Part B: Applied Biomaterials, 106(5) (2018) 1686-1697

[7] Kim, H.Y., Ikehara, Y., Kim, J.I., Hosoda, H., Miyazaki, S., Martensitic transformation, shape memory effect and superelasticity of Ti–Nb binary alloys, Acta Materialia, 54(9) (2006) 2419-2429.

[8] Hussein, M.A., Yilbas, B., Kumar, A.M., Drew, R., Al-Aqeeli, N., Influence of laser nitriding on the surface and corrosion properties of Ti-20Nb-13Zr alloy in artificial saliva for dental applications, Journal of Materials Engineering and Performance, 27(9) (2018) 4655-4664.

[9] Zhang, T., Fan, Q., Ma, X., Wang, W., Wang, K., Shen, P., Yang, J., Wang, L., Effect of laser remelting on microstructural evolution and mechanical properties of Ti-35Nb-2Ta-3Zr alloy, Materials Letters, 253 (2019) 310-313.

[10] Zhao, X., Liu, H., Li, S., Wang, X., Sheng, Y., Zhang, P., Li, W., Combined effect of TiN coating and surface texture on corrosion-wear behavior of selective laser melted CP-titanium in simulated body fluid, Journal of Alloys and Compounds, In Press, Corrected Proof.

[11] Katayama, S., Matsunawa, A., Morimoto, A., Ishimoto, S., Arata, Y., Surface hardening of titanium by laser nitriding. Journal of Laser Applications. 1983 (1983) 127-134.

[12] Kamat, A.M., Copley, S.M., Segall, A.E., Todd Copley, J. (2019). Laser-sustained plasma (LSP) nitriding of titanium: A review. Coatings, 9(5) (2019) 283.

[13] Chan, C.W., Carson, L., Smith, G.C., Morelli, A., Lee, S., Enhancing the antibacterial performance of orthopaedic implant materials by fibre laser surface engineering, Applied Surface Science, 404 (2017)a 67-81.

[14] Chan, C.W., Lee, S., Smith, G.C., Donaghy, C., Fibre laser nitriding of titanium and its alloy in open atmosphere for orthopaedic implant applications: Investigations on surface quality, microstructure and tribological properties, Surface and Coatings Technology, 309 (2017)b 628-640.

[15] Donaghy, C., McFadden, R., Kelaini, S., Carson, L., Margariti, A., Creating an antibacterial surface on beta TNZT alloys for hip implant applications by laser nitriding, Optics & Laser Technology, 121 (2020) 105793.

[16] Xue, L., Islam, M., Koul, A.K., Bibby, M., Wallace, W., Laser gas nitriding of Ti-6Al-4V Part 1: Optimization of the process. Advanced Performance Materials, 4 (1997) 25-47.

[17] Hu, C., Baker, T.N., The importance of preheat before laser nitriding a Ti–6Al–4V alloy. Materials Science and Engineering A, 265 (1999) 268-275.

[18]Mridha, S., Baker, T.N., Crack-free hard surfaces produced by laser nitriding of commercial purity titanium. Materials Science and Engineering A, 188 (1994) 229-239.
[19]Nwobu, A.I.P., Rawlings, R.D., West, D.R.F., Nitride formation in titanium based substrates during laser surface melting in nitrogen–argon atmospheres. Acta Materialia, 47 (1999) 631-643.
[20]Kaspar, J., Bretschneider, J., Jacob, S., Bonß, S., Winderlich, B., Brenner, B., Microstructure, hardness and cavitation erosion behaviour of Ti–6Al–4V laser nitrided under different gas atmospheres. Surface Engineering, 23 (2007) 99-106.
[21]Geetha, M., Mudali, U.K., Pandey, N.D., Asokamani, R., Raj, B., Microstructural and corrosion evaluation of laser surface nitrided Ti–13Nb–13Zr alloy, Surface Engineering, 20 (2004) 68-74.
[22]Diamanti, M.V., Del Curto, B. and Pedeferri, M., Interference colors of thin oxide layers on titanium. Color Research & Application, 33 (2008) 221-228.
[23]A.B. Kloosterman, J.Th.M. De Hosson, Microstructural characterization of laser nitrided titanium, Scripta Metallurgica et Materialia, 33(4) (1995) 567-573.
[24]Xin, H., Hu, C., Baker, T.N., Microstructural assessment of laser nitrided Ti-6Al-4V alloy, Journal of Materials Science, 35(13) (2000) 3373-3382.
[25]Man, H.C., Cui, Z.D., Yue, T.M., Cheng, F.T., Cavitation erosion behavior of laser gas nitrided Ti and Ti6Al4V alloy, Materials Science and Engineering: A, 355 (1–2) (2003) 167-173.
[26]Abboud, J.H., Fidel, A.F., Benyounis, K.Y., Surface nitriding of Ti–6Al–4V alloy with a high power CO2 laser, Optics & Laser Technology, 40(2) (2008) 405-414.
[27]Biswas, A., Li, L., Chatterjee, U.K., Manna, I., Pabi, S.K., Dutta Majumdar, J., Mechanical and electrochemical properties of laser surface nitrided Ti–6Al–4V, Scripta Materialia, 59(2) (2008) 239-242.
[28]Zhao, X., Zhang, P., Wang, X., Chen, Y., Liu, H., Chen, L., Sheng, Y., Li, W., In-situ formation of textured TiN coatings on biomedical titanium alloy by laser irradiation, Journal of the Mechanical Behavior of Biomedical Materials, 78 (2018) 143-153.
[29]International Centre for Diffraction Data, Newton Sq, PA, USA, PDF-2 Database.
[30]Sathish, S., Geetha, M., Pandey, N.D., Studies on the corrosion and wear behavior of the laser nitrided biomedical titanium and its alloys, Materials Science and Engineering C, 30(3) (2010) 376-382.
[31]Collings, E.W. (1984) The Physical Metallurgy of Titanium Alloys. American Society for Metals, Metals Park, OH
[32]Kim, H.Y., Miyazaki, S., Several Issues in the Development of Ti–Nb-Based Shape Memory Alloys, Shape Memory and Superelasticity 2(4) (2016) 380-390.
[33]Petch N.J., The cleavage strength of polycrystals, The Journal of the Iron and Steel Institute, 174 (1953) 25-28.